Virtual Damping Control Design of Three-Phase Grid-Tied PV Inverters for Passivity Enhancement

Zhiqing Yang, *Student Member, IEEE*, Chirag Shah, *Student Member, IEEE*, Tianxiao Chen, *Student Member, IEEE*, Jakob Teichrib, *Student Member, IEEE*, and Rik W. De Doncker, *Fellow, IEEE*

***Abstract*—The interconnection stability of a grid-tied inverter system can be investigated not only based on classical control theory, e.g., Nyquist criterion, but also from the energy dissipation point of view. If a critical resonance occurs within the regions, where the system equivalent impedance behaves passively, i.e., has only nonnegative real parts, the system stability can be guaranteed. Thus, it is preferred to design systems with passive regions over a wide-frequency range. This article investigates passivity properties influenced by different control loops and operating points in the dq frame, which facilitates the stability assessment in the frequency domain. Based on this, a virtual damping control method is proposed to improve the stability by enhancing the system passivity. By implementing a damping transfer function in the d- and q-axis individually, nonpassive regions can be accordingly reduced over a specific frequency range. Asymmetrical designs can be considered in the d- and q-axis according to corresponding passivity properties, which is impossible to be realized through symmetric physical filter components. The design procedure is elaborated based on a 2 MW inverter system, which is based on a combined graphical and analytical approach. Verifications are conducted based on a 1 kW prototype including both simulations and experimental results. The method applies to all types of grid-tied inverters with multiple control loops. This article is accompanied by a video demonstrating the validations.**

***Index Terms*—Control design, grid-tied converter, passivity, resonances, stability.**

I. Introduction

WIDE range resonances have been observed in large-scale photovoltaic (PV) parks from tens to thousands of hertz [1]. Poorly damped resonances can destabilize system operations especially under weak grid conditions [2]. Grid-tied PV inverter systems require different control loops to meet the requirements of the grid code in the distribution level [3], i.e., a phase-locked loop (PLL) for grid synchronization and a direct-voltage control (DVC) to realize the maximum-power-point tracking (MPPT) function. It is reported that negative incremental resistance exists within the bandwidth of a PLL, which can cause severe instability issues [4]. Nonoptimum design of a DVC can also lead to stability problems [5]. The delay caused by the digital control and modulation may also cause undesired resonances [6]. Hence, a proper methodology is necessary to explore the exact reason of unstable resonances.

To investigate the system stability and identify the reason of unstable resonances, two different methods are commonly used. The first method is eigenvalue-based stability analysis, where the system stability is investigated by the eigenvalues of a state-space model in the time domain [7]–[11]. The second method is impedance-based stability analysis based on an impedance model (IM) in the frequency domain, where a system is split into a source and a load subsystem. The stability is assessed by applying the Nyquist criterion on the source-load impedance ratio [12]–[14]. Discussions have been made to summarize and compare the two different methods [14]. However, both of the methods assess multivariable systems based on the classical control theory [15].

Apart from the control theory, the stability of a system can be also investigated from the energy dissipation point of view, which leads to the passivity theory. A system is defined as passive for a specific frequency range, if the real part of its transfer function is nonnegative in this frequency range [16]. The passivity of an inverter system is analyzed in [17] based on IMs, considering the influence of the alternating-current control (ACC), PLL, and DVC. However, the influence of different factors is analyzed separately neglecting the dynamic overlap between different control loops. In spite of the fact that the system is modeled with two-dimensional matrices, the passivity property influenced by asymmetrical control loops, i.e., DVC and PLL, is observed with only one diagonal element, which neglects the cross-coupling effect between the d- and q-axis. Detailed passivity analyses based on two-dimensional impedance matrices have not been considered.

Manuscript received July 1, 2020; revised September 13, 2020; accepted October 23, 2020. Date of publication November 3, 2020; date of current version February 5, 2021. This work was supported by the German Federal Ministry for Economic Affairs and Energy (BMWi, FKZ0324211D), PV-Kraftwerk2025. Recommended for publication by Associate Editor J. Liu. *(Corresponding author: Zhiqing Yang.)*

The authors are with the Institute for Power Generation and Storage Systems, E.ON Energy Research Center, RWTH Aachen University, 52074 Aachen, Germany (e-mail: zhiqing.yang@eonerc.rwth-aachen.de; chirag.shah@rwth-aachen.de; tianxiao.chen@rwth-aachen.de; jakob.teichrib@rwth-aachen.de; post_pgs@eonerc.rwth-aachen.de).

This article has supplementary downloadable material available at https://ieeexplore.ieee.org, provided by the authors.

Color versions of one or more of the figures in this article are available online at https://ieeexplore.ieee.org.

Digital Object Identifier 10.1109/TPEL.2020.3035417

Resonances can be dissipated when occurring within the frequency range, where the system behaves passively. Based on the passivity theory, control methods are developed to improve the stability by increasing the passivity regions. A passivity-based control design is developed for the ACC by adjusting the bandwidth of the voltage feedforward filter (VFF) [18]. However, the influence of the PLL and DVC is neglected. A coarse selection of the bandwidth for the PLL and DVC is provided in [17], based on the passivity property of diagonal admittances, though a design guideline is missing. Passivity-based designs are proposed to suppress the critical resonance caused by LCL filters [19]–[22] or control delay [23]. If an advanced modeling approach, i.e., multiple-frequency model is considered, it is possible to design a passive system even above the Nyquist frequency [24]. Passivity index is proposed to facilitate the design of the ACC from the control engineering point of view [25]. However, most studies model a three-phase system considering symmetric structures [18]–[24]. Such a system can be simplified to single-input single-output (SISO) structure, which requires only a one-dimensional IM for the passivity analysis. If asymmetric control loops, i.e., PLL and DVC, are considered, the system is featured with a multi-input multi-output (MIMO) structure. A two-dimensional IM established in a synchronous reference frame (SRF) is necessary to describe the complete system dynamics including the cross-coupling effect [17]. A control design guideline based on two-dimensional passivity properties of MIMO systems is still missing. Mathematical efforts are made to convert MIMO structures to SISO systems [26]. The stability is determined by the Nyquist plot of multiple control loops simultaneously. However, a control design approach to improve the system stability is not discussed.

To eliminate unstable resonances in converter-based systems induced by control interactions, the virtual damping technique is one of possible methods [27]. It is implemented to prevent the instability in both dc systems [28] and ac systems [29], [30]. Note that the virtual damping strategies developed in [28]–[30] have similar structures compared to the passivity-based control structures proposed in [19]–[22]. This indicates that the virtual damping technique eliminates critical resonances by essentially enhancing the system passivity. To prevent the dc-bus instabilities, a virtual damping strategy is proposed in [28] by utilizing a high-pass filter (HPF) to enhance the passivity in the medium-frequency region. The design is based on Nyquist plots without analytical guidelines. To tackle the instability caused by the PLL, a damping method is proposed to reshape the q-axis impedance by implementing a virtual resistor [29]. However, the relationship between the virtual damping and the passivity property is not elaborated. Due to the model simplification, there is no discussion with regard to other control loops, e.g., ACC, DVC, and VFF. A design guideline is provided in [29], where the value of the virtual resistor is dependent on the operation point. Whether the design can guarantee robust operations in a wide range, is not discussed. A virtual inductor in series to the grid impedance is considered in [30] to enhance the stability under weak grid conditions. However, the model neglects the influence of the PLL, which may not guarantee the accuracy when investigating the stability issue for weak grid scenarios. The cause of unstable resonances is not well identified, so that a design guideline is not considered.

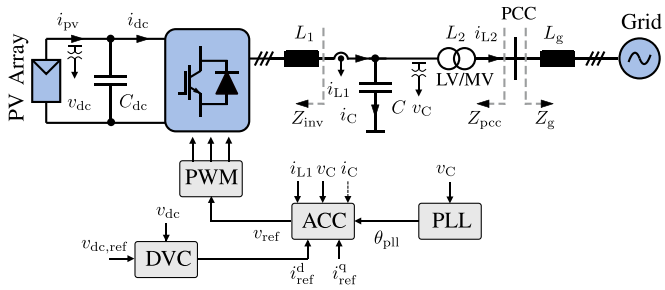

Fig. 1. System configuration of a three-phase PV inverter.

To cope with the control-induced unstable resonances, this article develops a framework to assess and improve the passivity of three-phase grid-tied PV inverters by utilizing the virtual damping technique. Main contributions are summarized as follows.

a) Concrete passivity analysis is conducted based on two-dimensional IMs. Passivity properties influenced by different control loops and operating points are assessed in the dq frame. Asymmetric passivities are observed in the d- and q-axis, so that the cause of unstable resonances can be identified.

b) A virtual damping control (VDC) method is proposed to improve system stability by enhancing the passivity property in the d- and q-axis individually. A design guideline based on the combined graphical and analytical approach is provided and the effectiveness of the VDC is validated.

The rest of this article is organized as follows. In Section II, an accurate IM is developed for a three-phase grid-tied PV inverter system considering complete dynamics of different control loops. The passivity-based stability analysis method is introduced and applied to the established system to explain the cause of unstable resonances. Passivity properties are thoroughly analyzed in Section III for different control loops and operating points, considering also the influence of cross-coupling effects in the dq frame. To improve the system stability, a VDC design is proposed in Section IV by enhancing the system passivity. The virtual damping is implemented in the d- and q-axis diagonal element asymmetrically, so that the nonpassive regions can be accordingly reduced over a wide-frequency range. A design guideline is provided, based on which the VDC is designed for a 2 MW system. Verifications are provided in Section V with both simulations and experimental results based on a down-scale prototype. The conclusion is drawn in Section VI.

II. Stability Assessment of Grid-Tied Inverters

A. Impedance Model

The three-phase grid-tied PV inverter shown in Fig. 1 is considered for the analysis. An LCL filter is implemented for the harmonic suppression, where L_2 is realized by the leakage inductance of a step-up transformer. The ACC is implemented

TABLE I
SYSTEM AND CONTROL PARAMETERS OF 2-MW SYSTEM

Parameter	Value	Parameter	Value
$V_{\mathrm{g,ll}}^{\mathrm{rms}}$	550 V	P_{n}	2 MW
f_{sw}	3 kHz	f_{sp}	6 kHz
V_{dc}	1200 V	f_{g}	50 Hz
C_{dc}	15 mF	L_1	120 µH
C	1 mF	L_2	40 µH
$f_{\mathrm{bw}}^{\mathrm{ACC}}$	300 Hz	$K_{\mathrm{p}}^{\mathrm{ACC}}$	0.23 Ω
$f_{\mathrm{bw}}^{\mathrm{PLL}}$	30 Hz	$K_{\mathrm{p}}^{\mathrm{PLL}}$	0.36 rad/sV
$f_{\mathrm{bw}}^{\mathrm{DVC}}$	20 Hz	$K_{\mathrm{p}}^{\mathrm{DVC}}$	3.6 S

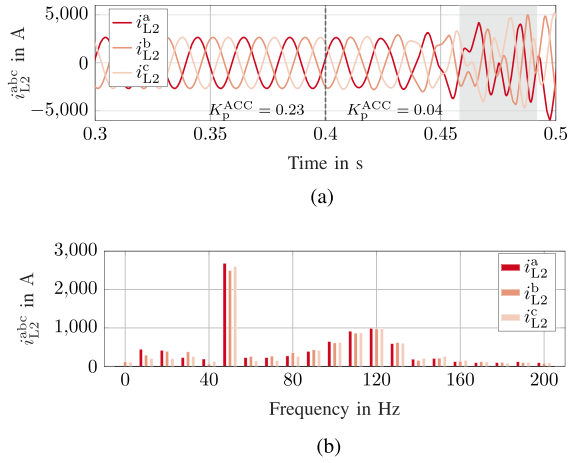

Fig. 2. Analysis of i_{L2} for a step change of K_p^{ACC}. (a) Time-domain analysis. (b) Frequency-domain analysis.

as the inner control loop considering the VFF and AD. The capacitor voltages in the LCL filter are measured for the grid synchronization with a SRF-based PLL. The DVC is implemented to realize the MPPT. The system delay caused by digital control and zero-order hold (ZOH) effect is also considered. An IM is developed for the described system. The stability can be assessed by applying the general Nyquist criterion (GNC) to the impedance ratio as given in (1) [12], where Z_{pcc} and Z_g represent the inverter-side and grid-side impedance at the point of common coupling as marked in Fig. 1. The impedance Z_{pcc} is acquired by combining the inverter output admittance Y_{inv} and the filter impedance or admittance as given in (2), where Y_C and Z_{L2} are the capacitor admittance and the inductor impedance in the LCL filter. The inverter admittance Y_{inv} is calculated according to the small-signal relationship of ac-side currents and voltages, which depends on the implemented control loops and operating points. As the IM is established in the dq frame, the admittance is represented by a two-dimensional matrix as given in (3). Derivations of the complete IM are provided in Appendix A

$$T = Z_{\mathrm{pcc}}^{-1} \cdot Z_g = Y_{\mathrm{pcc}} \cdot Z_g \tag{1}$$

$$Z_{\mathrm{pcc}} = (Y_{\mathrm{inv}} + Y_C)^{-1} + Z_{L2} \tag{2}$$

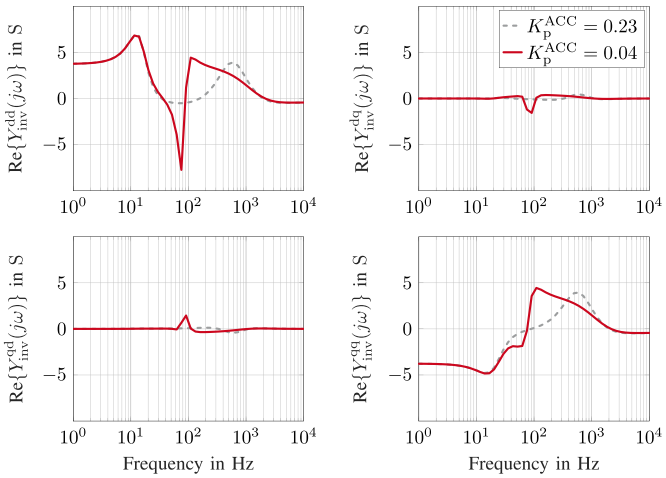

Fig. 3. Passivity properties influenced by K_p^{ACC}.

$$Y_{\mathrm{inv}}(s) = \begin{bmatrix} Y_{\mathrm{inv}}^{dd}(s) & Y_{\mathrm{inv}}^{dq}(s) \\ Y_{\mathrm{inv}}^{qd}(s) & Y_{\mathrm{inv}}^{qq}(s) \end{bmatrix}. \tag{3}$$

B. Passivity-Based Stability Assessment

In addition to the GNC, the stability of a system can be also assessed from the energy dissipation point of view, which leads to the passivity theory. A system $G(s)$ is defined to be passive if $\mathrm{Re}\{G(j\omega)\} \geq 0$, $\forall\, \omega$ [16], which represents a nonnegative impedance or admittance for an electrical system. A passive system is able to remain stable by dissipating the undesired energy such as resonances. For the established IM, the stability can be assessed by investigating the passivity of the inverter admittance Y_{inv}, as the filter components C, L_2 and the grid impedance L_g are passive naturally.

To reveal the relationship between unstable resonances and passivity properties, an example is presented based on simulations in PLECS for a central PV inverter with parameters given in Table I. The system is stable with the properly designed proportional gain in the ACC $K_p^{\mathrm{ACC}} = 0.23$. Unstable resonances occur if the gain is reduced to $K_p^{\mathrm{ACC}} = 0.04$ as illustrated in Fig. 2 for the current i_{L2} in both the time-domain and frequency-domain. To identify the cause of unstable resonances, the two-dimensional passivity properties of Y_{inv} are depicted in Fig. 3. Several findings are summarized as follows.

1) In spite of the fact that a clear nonpassive area is observed in Y_{inv}^{qq} in the low-frequency range and small nonpassive regions exist in Y_{inv}^{dd}, Y_{inv}^{dq}, and Y_{inv}^{qd}, the system is stable with $K_p^{\mathrm{ACC}} = 0.23$. The reason is that, the passivity theory provides a sufficient but not necessary condition to analyze the stability. Nonpassive regions do not directly indicate instabilities. Unstable resonances appear if excitations occur within nonpassive regions. Therefore, the passivity theory is often used for control design to improve the system stability by reducing the nonpassive regions [18]–[25]. While the Bode plots and Nyquist criterion are

often used to predict whether a system is stable or not [4], [12]–[14].

2) Diagonal passivities $\mathrm{Re}\{Y_{\mathrm{inv}}^{dd}(j\omega)\}$ and $\mathrm{Re}\{Y_{\mathrm{inv}}^{qq}(j\omega)\}$ are nonidentical, which indicates the asymmetry between the d- and q-axis. While off-diagonal passivities $\mathrm{Re}\{Y_{\mathrm{inv}}^{dq}(j\omega)\}$ and $\mathrm{Re}\{Y_{\mathrm{inv}}^{qd}(j\omega)\}$ are identical with a minus sign. The absolute value of off-diagonal passivities are much smaller than the diagonal ones. The passivity variations of off-diagonal elements over a wide-frequency range are negligible compared to diagonal elements. The reason is that, cross-coupling effects in the dq frame are compensated, and the operation is assumed with a high power factor. In this case, the stability of three-phase ac systems can be investigated with a focus on diagonal elements, which is valid for both rectifier-mode [31] and inverter-mode [32] operations.
3) For $K_p^{\mathrm{ACC}} = 0.04$, a steep nonpassive region occurs in Y_{inv}^{dd} with a minimum damping of -8S between $60-70$ Hz, which matches the dominant resonances observed in Fig. 2(b) between $110-120$ Hz, considering a frequency shift of 50 Hz from the dq to the abc frame. In the same frequency range between $60-70$ Hz, the minimum passivity of Y_{inv}^{dq} and Y_{inv}^{qq} are -1.5 and -2S, respectively. While the passivity of Y_{inv}^{qd} is 0S. The worst damping of Y_{inv}^{qq} is -5S between 10 and 20 Hz, which already exists even with the normal gain $K_p^{\mathrm{ACC}} = 0.23$. Moreover, the observed resonances do not match this frequency range. Thus, it can be concluded that the nonpassive region in Y_{inv}^{dd} is the major cause of unstable resonances in this case.

III. Two-Dimensional Passivity Analysis

Ideally, a stable system requires the nonnegative admittance $\mathrm{Re}\{Y_{\mathrm{inv}}(j\omega)\} \geq 0$ over the whole frequency range. However, it is impossible for the grid-tied inverters due to the implemented control loops. To identify the exact cause of the nonpassive regions, the two-dimensional passivity properties influenced by different factors are investigated as follows based on the system specifications in Table I.

A. Control Delay

Due to the implementation of digital control and the ZOH effect of the pulsewidth modulation (PWM), there is an inevitable system delay T_{del} between the control command and inverter output voltage. A minimum delay of $T_{\mathrm{del}} = 1.5\,T_{\mathrm{sp}}$ with the sampling time T_{sp} is considered for the double-update PWM [23]. The passivities influenced by control delay are observed in Fig. 4. Note that a nonzero T_{del} causes an inevitable nonpassive region in the high-frequency region above 1 kHz in both Y_{inv}^{dd} and Y_{inv}^{qq}. The nonpassive region increases with a higher value of delay. However, it has no influence on the low-frequency regions. An increased delay time slightly influences the passivity of Y_{inv}^{dq} and Y_{inv}^{qd} near the ACC bandwidth. However, the influence is negligible compared to the influence on diagonal passivities, if a reasonable delay time is considered.

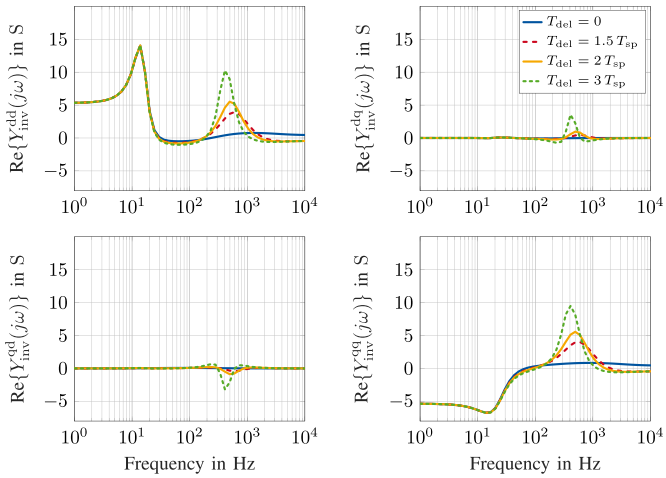

Fig. 4. Passivity properties influenced by the control delay.

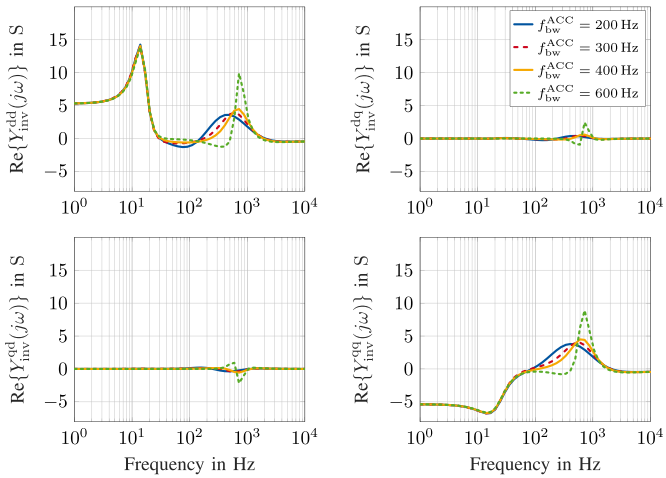

Fig. 5. Passivity properties influenced by the ACC.

B. Alternating-Current Control

Different bandwidths of the ACC $f_{\mathrm{bw}}^{\mathrm{ACC}}$ mainly influence the medium-frequency region between $50-500$ Hz for both Y_{inv}^{dd} and Y_{inv}^{qq} as illustrated in Fig. 5. A high value of the ACC bandwidth introduces nonpassive regions in both dq-axis, as it is close to the switching frequency $f_{\mathrm{sw}} = 3$ kHz. While a low value of the ACC bandwidth induces a nonpassive region only in the d-axis, as it is close to the DVC bandwidth $f_{\mathrm{bw}}^{\mathrm{DVC}} = 20$ Hz. Thus, $f_{\mathrm{bw}}^{\mathrm{ACC}} \approx \frac{f_{\mathrm{sw}}}{10}$ is usually considered as a rule of thumb [17]. The influence on Y_{inv}^{dq} and Y_{inv}^{qd} is negligible if a reasonable ACC bandwidth is implemented.

C. Voltage Feedforward Filter

The bandwidth of the VFF $f_{\mathrm{bw}}^{\mathrm{VFF}}$ has influence on the system stability especially under weak grid conditions. It is suggested to have a small VFF bandwidth $f_{\mathrm{bw}}^{\mathrm{VFF}} \leq 0.1\, f_{\mathrm{bw}}^{\mathrm{ACC}}$ in normal operations to enhance the stability [18]. However, this is only a coarse design and the lower limitation of the VFF bandwidth is not

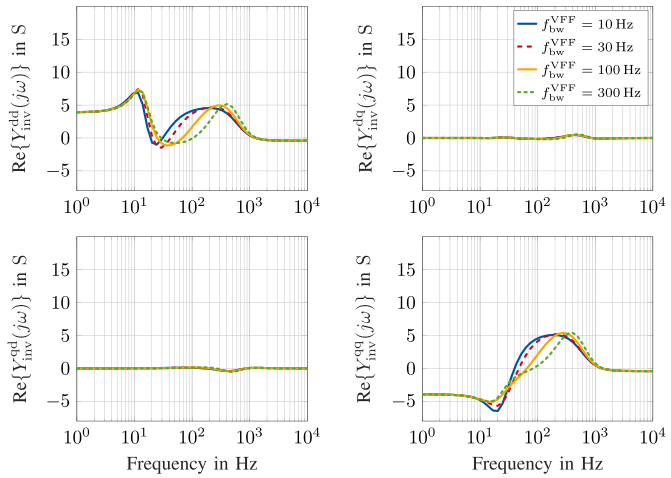

Fig. 6. Passivity properties influenced by the VFF.

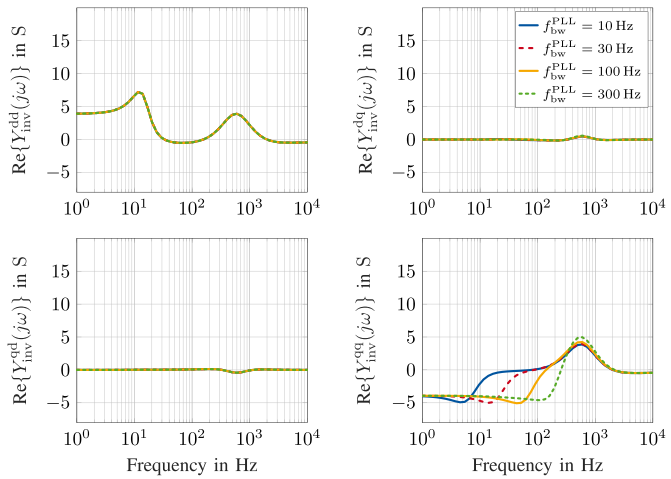

Fig. 7. Passivity properties influenced by the PLL.

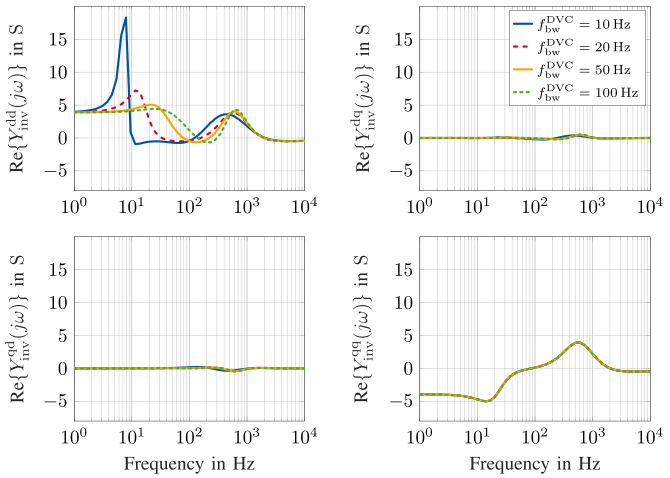

Fig. 8. Passivity properties influenced by the DVC.

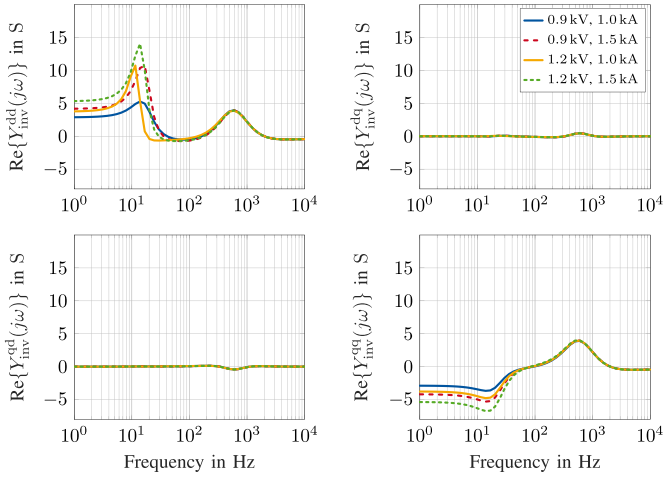

Fig. 9. Passivity properties influenced by the MPPT.

considered. As shown in Fig. 6, the VFF bandwidth influences the passivity property in a wide-frequency range. A small bandwidth reduces the nonpassive region in the low-frequency range of Y_{inv}^{dd} and improves the passivity in the medium-frequency range of Y_{inv}^{qq}. However, the negative damping of Y_{inv}^{qq} in the low-frequency region gets deteriorated. As a compromise, it is recommended to select $f_{\mathrm{bw}}^{\mathrm{VFF}} = 0.1 - 0.3\, f_{\mathrm{bw}}^{\mathrm{ACC}}$ to guarantee the wide-range passivity. The influence on Y_{inv}^{dq} and Y_{inv}^{qd} is negligible.

D. Phase-Locked Loop

The passivity properties influenced by the PLL bandwidth $f_{\mathrm{bw}}^{\mathrm{PLL}}$ are depicted in Fig. 7. Note that a PLL mainly influences Y_{inv}^{qq}, as it regulates only v_C^q for grid synchronization. An inevitable nonpassive region occurs within the PLL bandwidth, which has been reported in [13] and [14]. Thus, it is recommended not to select the bandwidth of PLL unnecessarily large. The PLL bandwidth has no influence on Y_{inv}^{dd} and the influence on Y_{inv}^{dq} and Y_{inv}^{qd} is negligible.

E. DVC Loop

The passivity properties influenced by the DVC bandwidth $f_{\mathrm{bw}}^{\mathrm{DVC}}$ are illustrated in Fig. 8. On contrary to a PLL, a DVC influences mainly Y_{inv}^{dd}, as it provides only a d-axis reference current for the ACC. A nonpassive region occurs in the frequency range slightly above the DVC bandwidth. A high DVC bandwidth reduces the total nonpassive region in Y_{inv}^{dd}. It is suggested in [17] to select the DVC bandwidth as $f_{\mathrm{bw}}^{\mathrm{DVC}} \leq 0.1\, f_{\mathrm{bw}}^{\mathrm{ACC}}$. However, a lower limitation should be also considered. A small DVC bandwidth increases the nonpassive region within its bandwidth, which deteriorates the system damping in the low-frequency range. The DVC bandwidth has no influence on Y_{inv}^{qq} and the influence on Y_{inv}^{dq} and Y_{inv}^{qd} is negligible.

F. Maximum Power-Point Tracking

Different operating points due to the MPPT function affect passivity properties as well. Both the PV current I_{pv} and the dc-link voltage V_{dc} vary in a wide range due to the MPPT function. The influences of different I_{pv} and V_{dc} are presented in Fig. 9.

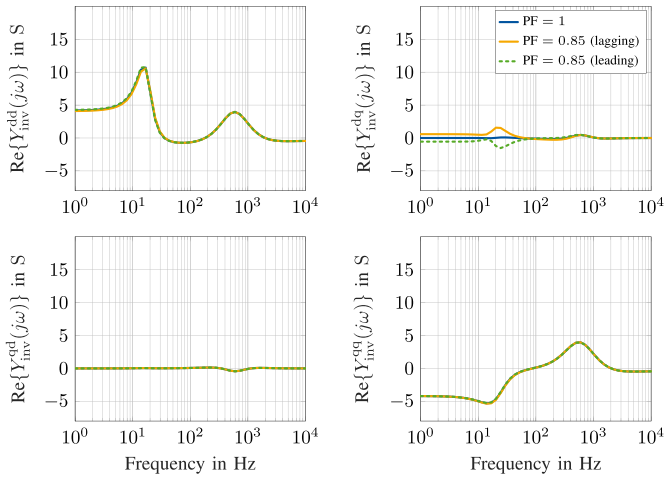

Fig. 10. Passivity properties influenced by the PF.

A high PV current $I_{\rm pv}$ enhances the low-frequency passivity in $Y_{\rm inv}^{dd}$, while deteriorates the nonpassive region caused by the PLL in $Y_{\rm inv}^{qq}$. A similar trend is observed if a high dc-link voltage $V_{\rm dc}$ is implemented. Thus, a limitation of $I_{\rm pv}$ shall be considered to guarantee stable operations. Different operating points have almost no influence on $Y_{\rm inv}^{dq}$ and $Y_{\rm inv}^{qd}$.

G. Power Factor

The grid code requires PV inverters to operate with a power factor PF > 0.85 (leading or lagging) when the output power is higher than 10% of its nominal rating [33]. Specially designed systems that provide reactive power compensation, e.g., STATCOM, are out of the scope of this work. The passivity properties influenced by the PF are depicted in Fig. 10. The passivity of $Y_{\rm inv}^{dq}$ slightly increases with a lagging PF below the PLL bandwidth, while it decreases with a leading PF. Different PFs have almost no influence on $Y_{\rm inv}^{dd}$, $Y_{\rm inv}^{qd}$, and $Y_{\rm inv}^{qq}$.

H. Grid Impedance

According to (30), the passivity of an inverter depends only on its own parameters and operating conditions. The grid impedance does not influence the inverter passivity. Thus, corresponding figures are not provided. However, a change of the grid impedance shifts the resonant frequency, which can be analyzed with Bode plots [12]. Unstable resonances occur if the resonant frequency falls into the nonpassive region.

In summary, passivity properties are different between diagonal elements $Y_{\rm inv}^{dd}$ and $Y_{\rm inv}^{qq}$, which indicates asymmetric features mainly caused by the PLL and DVC. Nonpassive regions mainly exist in diagonal elements $Y_{\rm inv}^{dd}$ and $Y_{\rm inv}^{qq}$, while passivity properties of off-diagonal elements $Y_{\rm inv}^{dq}$ and $Y_{\rm inv}^{qd}$ are negligible, if proper designs are considered.

IV. Virtual Damping Control

The passivity theory offers an intuitive approach to analyze unstable resonances in the frequency domain. Nonpassive regions can exist in all elements in the admittance matrix $Y_{\rm inv}$ even with proper designs of the control loops. To improve the system stability, it is preferred to reduce the nonpassive region as much as possible. Hence, a VDC method is proposed to enhance the system passivity. The control structure and design approach are elaborated in this section. The method is aimed for reducing the control-induced nonpassive regions below 1 kHz. The nonpassive regions above 1 kHz caused by the delay effect is out of the scope of this work.

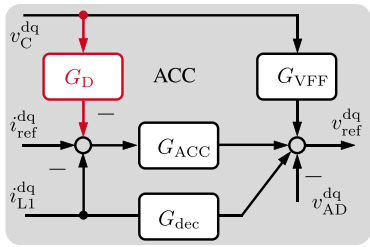

Fig. 11. Control structure with virtual damping.

A. Control Structure

Since a nonpassive region behaves like a negative resistance, a positive damping is necessary to remain the stability. As reported in [20]–[22], [29], and [30], a virtual damping can be implemented by adding a transfer function from the measured voltages or currents to the control loops. Utilizing a similar approach, the transfer matrix G_D is considered in the ACC to introduce a virtual damping as depicted in Fig. 11. According to the passivity analysis in Section III, nonpassive regions are mainly caused by diagonal elements, and the passivity of off-diagonal elements are negligible. Hence, the damping matrix is designed in a diagonal format as given in (4). With zero values of off-diagonal elements, G_D^{dd} has no influence on the $Y_{\rm inv}^{qq}$, while G_D^{qq} has no influence on $Y_{\rm inv}^{dd}$, which facilitates the passivity design in the d- and q-axis individually

$$G_D(s) = \begin{bmatrix} G_D^{dd}(s) & 0 \\ 0 & G_D^{qq}(s) \end{bmatrix}. \tag{4}$$

Different types of transfer functions of G_D are compared to find the best solution, which includes the HPF, the low-pass filter (LPF) and the proportional-integral (PI) structure.

1) High-Pass Filter: Considering the transfer function in (5) for both G_D^{dd} and G_D^{qq}, passivity properties of $Y_{\rm inv}^{dd}$ and $Y_{\rm inv}^{qq}$ are observed in Fig. 12, where $\omega_{\rm HPF} = 2\pi f_{\rm HPF}$ represents the cut-off frequency and K is the gain of the HPF. The influence of bandwidth is first investigated. A low bandwidth can slightly improve the passivity in the medium-frequency range for both $Y_{\rm inv}^{dd}(s)$ and $Y_{\rm inv}^{qq}(s)$. If a gain is further increased, the passivity in the medium-frequency range can be improved. However, passivity dips appear in both high-frequency and low-frequency regions. The HPF has no improvements to the nonpassive region

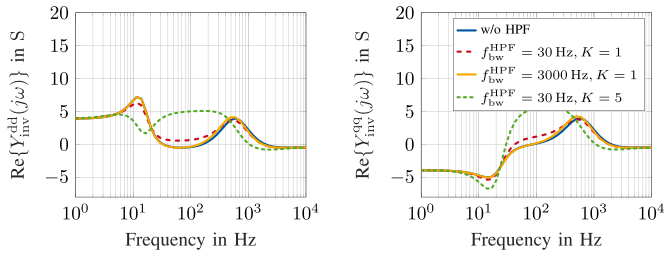

Fig. 12. Passivity properties with different HPFs.

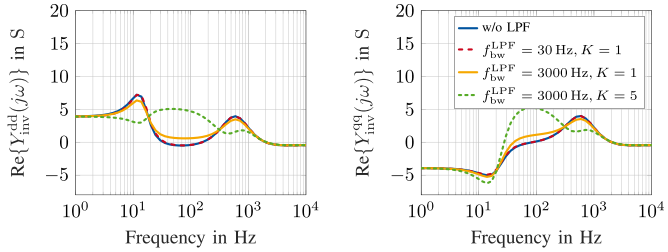

Fig. 13. Passivity properties with different LPFs.

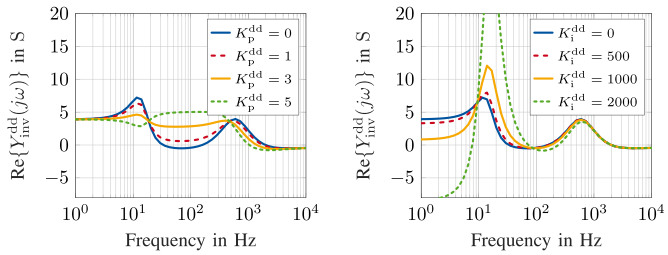

Fig. 14. Passivity properties of $Y_{\rm inv}^{dd}$ with different PI gains.

of $Y_{\rm inv}^{qq}$ in the low-frequency range

$$G_D^{\rm HPF} = \frac{sK}{s+\omega_{\rm HPF}}. \tag{5}$$

2) Low-Pass Filter: Considering the LPF given in (6), where $\omega_{\rm LPF} = 2\pi f_{\rm LPF}$ represents the cut-off frequency and K is the gain of the LPF. Passivity properties of both $Y_{\rm inv}^{dd}$ and $Y_{\rm inv}^{qq}$ are improved in the medium-frequency range with a high bandwidth as shown in Fig. 13. If the gain is further increased, the passivity in the medium-frequency range further increases, while passivity dips appear in both high-frequency and low-frequency regions. Moreover, the LPF cannot compensate the nonpassive region in the low-frequency range of $Y_{\rm inv}^{qq}$ either

$$G_D^{\rm LPF} = \frac{\omega_{\rm LPF}K}{s+\omega_{\rm LPF}}. \tag{6}$$

3) PI Controller: A PI controller given in (7) is discussed in-depth for the comparison. The passivity of $Y_{\rm inv}^{dd}$ is investigated with different PI gains of G_D^{dd}. As illustrated in Fig. 14, with an increased proportional gain K_p^{dd}, the nonpassive region in $Y_{\rm inv}^{dd}$ is alleviated. However, K_p^{dd} should not be selected too high to prevent the passivity dip below the DVC bandwidth. An increased integral gain K_i^{dd} enhances the passivity of $Y_{\rm inv}^{dd}$ in the

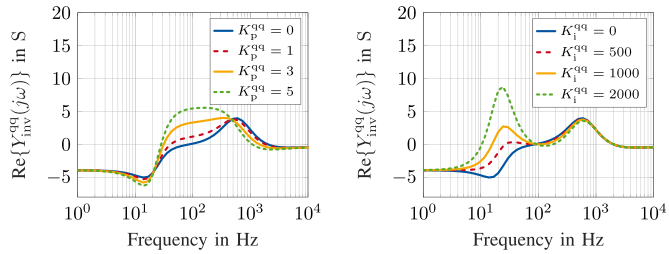

Fig. 15. Passivity properties of $Y_{\rm inv}^{qq}$ with different PI gains.

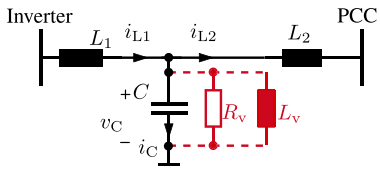

Fig. 16. Equivalent circuit with virtual damping.

medium-frequency range. However, it deteriorates the passivity in the low-frequency range either. Hence, only K_p^{dd} is considered in G_D^{dd}. Note that G_D^{dd} has no influence on $Y_{\rm inv}^{qq}$

$$G_D^{\rm PI} = K_p + \frac{K_i}{s}. \tag{7}$$

Similarly, the passivity of $Y_{\rm inv}^{qq}$ is analyzed with different PI gains of G_D^{qq} as illustrated in Fig. 15. The proportional gain K_p^{qq} improves the passivity in the medium-frequency range, while the integral gain K_i^{qq} alleviates the nonpassive region in the low-frequency caused by the PLL. Both the K_p^{qq} and K_i^{qq} do not deteriorate the passivity in other frequency ranges. Hence, both K_p^{qq} and K_i^{qq} are considered in G_D^{qq}. Note that G_D^{qq} has no influence on $Y_{\rm inv}^{dd}$.

Based on the analysis, the PI control structure achieves the best performance for both G_D^{dd} and G_D^{qq}. From the electrical point of view, the PI structure given in (7) can be rewritten as (8), which represents exactly a virtual admittance including a virtual resistor R_v and a virtual inductor L_v, for the d- and q-axis, respectively, as illustrated in Fig. 16. A high damping gain indicates a small value of either R_v or L_v. Thus, the nonpassive regions are essentially compensated by creating a "virtual short circuit" in a specific frequency range. The electrical equivalence facilitates the parameter selections, which will be discussed as follows:

$$G_D^{\rm ele} = \frac{1}{R_v} + \frac{1}{sL_v}. \tag{8}$$

B. Design Procedure

To determine the parameters of the proposed VDC, a design procedure is provided combining both the graphical and analytical approaches. Based on the passivity properties shown in Figs. 14 and 15, G_D^{dd} and G_D^{qq} can be designed separately. The detailed design flow chart is given in Fig. 17.

For the design of G_D^{dd}, only the proportional gain K_p^{dd} is required. The parameter is determined with the help of the

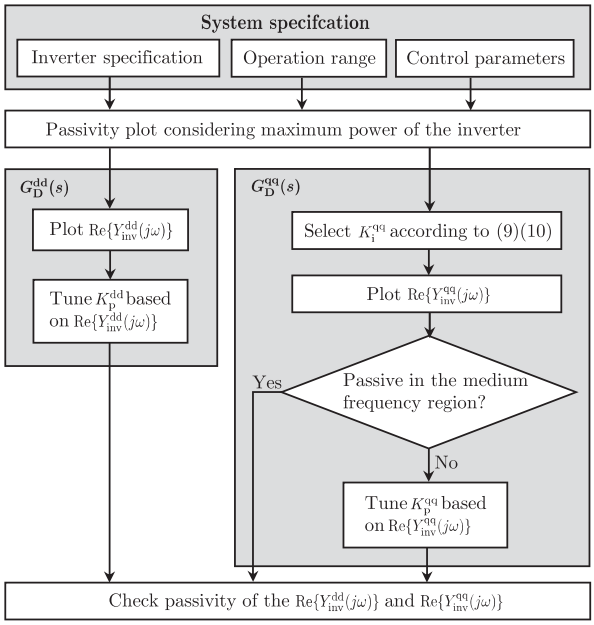

Fig. 17. VDC design procedure.

TABLE II
DESIGN OF VDC PARAMETERS FOR 2 MW SYSTEM

Parameter	Value	Parameter	Value
P_n	2 MW	K_p^{dd}	2 S
$V_{g,ll}^{rms}$	550 V	K_i^{qq}	2080 S/s
L_B	480 µH	K_p^{qq}	2 S

passivity plot. A proper K_p^{dd} is considered when the nonpassive region in Y_{inv}^{dd} is eliminated.

For the design of G_D^{qq}, both the K_p^{qq} and K_i^{qq} are required. As the integral gain K_i^{qq} achieves a better performance to compensate the nonpassive region in the low-frequency area caused by the PLL, it is considered first. According to (8), K_i^{qq} can be regarded as a parallel virtual inductor L_v. A proper value can be determined similar to the base impedance calculation as given in (9), which takes the inverter power rating P_n and the grid voltage level $V_{g,ll}^{rms}$ into account. Whereby, K_i^{qq} is calculated according to L_v as given in (10). As illustrated in Fig. 15, a passivity dip is introduced when implementing K_i^{qq}. Thus, a proportional gain K_p^{qq} is preferred to enhance the nonpassive region in the medium-frequency range, which is determined based on the passivity plot

$$L_v = \frac{V_B^2}{\omega_g S_B} = \frac{(V_{g,ll}^{rms})^2}{\omega_g P_n} \tag{9}$$

$$K_i^{qq} = \frac{1}{L_v}. \tag{10}$$

C. Design Case

A design case is presented based on the analyzed 2 MW PV inverter. Following the design procedure provided in Fig. 17, VDC parameters are designed and listed in Table II.

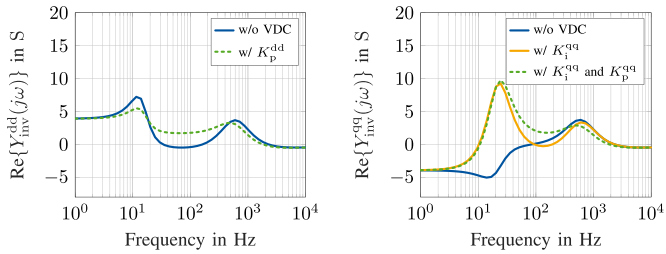

Fig. 18. Passivity enhancement with the designed VDC.

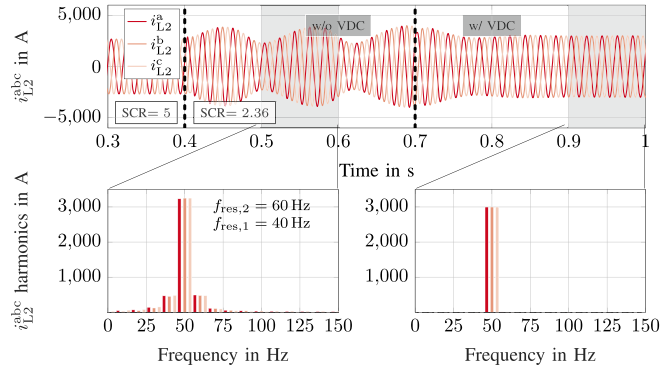

Fig. 19. Current waveform with step changes of SCR.

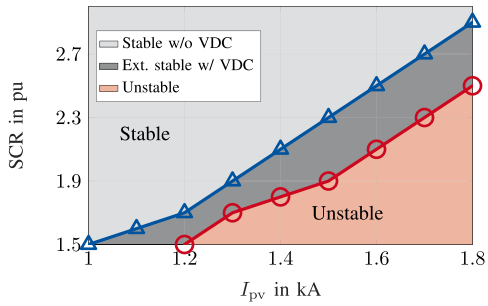

Fig. 20. Stability range extension.

Originally, nonpassive regions are observed in both Y_{inv}^{dd} and Y_{inv}^{qq} as depicted in Fig. 18. Unstable resonances occur if the short-circuit ratio (SCR) decreases from 5.0 to 2.36, as shown in Fig. 19. Resonances are observed at 40 and 60 Hz in the abc frame, which corresponds to 10 Hz in the dq frame considering the frequency shift and coupling effect [34]. After implementing the designed parameters, the passivity of both Y_{inv}^{dd} and Y_{inv}^{qq} are significantly enhanced as illustrated in Fig. 18. In spite of that the nonpassive region in Y_{inv}^{qq} cannot be completely eliminated, a nonnegative admittance is guaranteed above 10 Hz. As a result, the resonances that occurred in the passive region disappear. With the proposed VDC, stable operations can be extended under harsh conditions with either a low SCR or a high PV current. The extended stability boundary validated in simulations is illustrated in Fig. 20.

The proposed VDC is compared to other methods in previous studies as summarized in Table III. Different from other methods

TABLE III
DIFFERENT VIRTUAL DAMPING METHODS TO PREVENT THE INSTABILITY INDUCED BY CONTROL INTERACTIONS

Reference	Stability Assessment	Analyzed Influences	Damping Method	Design Guideline
[28]	Nyquist plot	DVC	HPF	Graphic assisted
[29]	Bode plot of $Z_{\rm g}^{\rm qq}/Z_{\rm pcc}^{\rm qq}$	PLL, $L_{\rm g}$	P gain ($R_{\rm v}$)	$K_{\rm p}=-\left(\frac{1}{K_{\rm p}^{\rm ACC}}+\frac{I_{\rm L1}^{\rm d}}{V_{\rm g}^{\rm d}}\right)$
[30]	Eigenvalue loci	$L_{\rm g}$	$L_{\rm v}$	Not addressed
Proposed	Two-dimensional passivity $Y_{\rm inv}^{\rm dq}$	PLL, DVC, ACC, $L_{\rm g}$, $I_{\rm pv}$	PI gains ($R_{\rm v}$, $L_{\rm v}$)	Graphic assisted and (9), (10)

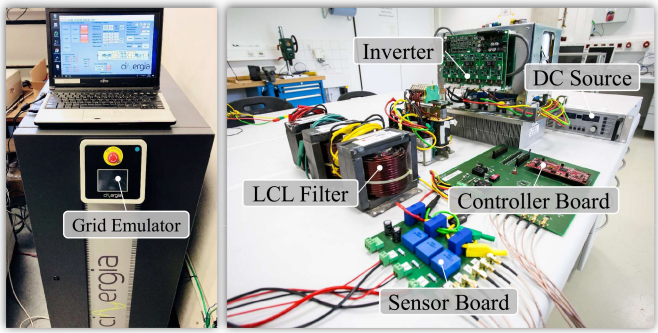

Fig. 21. Experimental setup.

TABLE IV
SYSTEM AND CONTROL PARAMETERS OF 1-kW SYSTEM

Parameter	Value	Parameter	Value
$V_{\rm g,ll}^{\rm rms}$	90 V	$P_{\rm n}$	1 kW
$f_{\rm sw}$	10 kHz	$f_{\rm sp}$	20 kHz
$V_{\rm dc}$	180 V	$f_{\rm g}$	50 Hz
C	10 µF	L_1	3 mH
$f_{\rm bw}^{\rm ACC}$	1 kHz	$K_{\rm p}^{\rm ACC}$	16 Ω
$f_{\rm bw}^{\rm PLL}$	30 Hz	$K_{\rm p}^{\rm PLL}$	2.3 rad/sV
$K_{\rm p}^{\rm qq}$	0.04 S	$K_{\rm i}^{\rm qq}$	40 S/s

TABLE V
EXPERIMENT SCENARIOS

Cases	$i_{\rm ref}^{\rm d}$	$L_{\rm g}$	PF	Cause of resonances
Case 1	10 A	3 mH (SCR = 7)	Unity	High $f_{\rm bw}^{\rm PLL}$
Case 2	6 A	5.5 mH (SCR = 4)	Unity	High $f_{\rm bw}^{\rm PLL}$
Case 3	6 A	3 mH (SCR = 7)	0.87	High $f_{\rm bw}^{\rm PLL}$
Case 4	10 A	3 mH (SCR = 7)	Unity	High $K_{\rm p}^{\rm qq}$

based on the classical control theory, e.g., Nyquist plots or eigenvalues, the proposed method investigates the stability utilizing two-dimensional passivity properties. The passivity theory provides a sufficient but not necessary condition for stability assessment, which cannot directly predict whether the system is stable or not. However, it provides an intuitive perspective to present the system damping feature over a wide-frequency range. By utilizing the two-dimensional passivity properties based on accurate IMs, resonances caused by control interactions of different loops can be identified and accordingly compensated. A design guideline is addressed combining the mathematical analysis and the graphical assisted method. Besides, the proposed VDC features following advantages.

1) No physical components are required, which leads to high efficiency of the system.
2) Asymmetric designs in the d- and q-axis compensate nonpassive regions caused by different controls flexibly.
3) The damping parameters are designed considering the maximum power rating. Thus, the stability is guaranteed in normal operations as well.

V. SIMULATION AND EXPERIMENTAL VALIDATION

To further investigate the validity of the proposed VDC, simulations and experiments are conducted based on a 1 kW prototype. The test setup is comprised of a three-phase inverter, a commercial grid emulator, a dc source, control, and sensor boards as well as an LCL filter, as shown in Fig. 21. The system and control parameters for the down-scale test setup are specified in Table IV. Based on the design procedure proposed in Fig. 17, VDC parameters are designed for the prototype and given in Table IV as well. Since no DVC is implemented in the down-scale prototype, there is no nonpassive region observed in $Y_{\rm inv}^{dd}$. Hence, only the q-axis virtual damping parameters are designed and implemented. There are in total four different cases considered in validations, detailed scenarios of which are defined in Table V.

A. Case 1

The case 1 validates the effectiveness of the VDC under normal grid operations with SCR = 7. Due to limited filter components available in the laboratory, an unstable scenario is emulated by intentionally increasing the PLL bandwidth, which extends the nonpassive region in $Y_{\rm inv}^{qq}$ to the medium-frequency range as depicted in Fig. 7. The system loses the stability if the PLL bandwidth increases to 170 Hz, where current distortions can be observed, as presented in Fig. 22(a). Resonances can be eliminated after implementing the proposed VDC. Note that the stability remains with a normal PLL bandwidth of 30 Hz, if the VDC is activated. Experimental results of case 1 are shown in Fig. 22(b). The current distortion is more severe in the hardware test, which is reasonable as the dead-time effect and parasitic parameters of the test bench are not fully considered in simulations. The frequency-domain analysis of the experimental results is observed for the unstable operation in Fig. 22(c). Passivity properties of $Y_{\rm inv}^{qq}$ acquired by the developed IM are plotted as well. Dominant resonances measured in the experiment occur at 190 and 290 Hz in the abc frame. This corresponds to the resonance at 240 Hz in the dq frame, which exactly falls into the nonpassive region if the VDC is not activated. The passivity

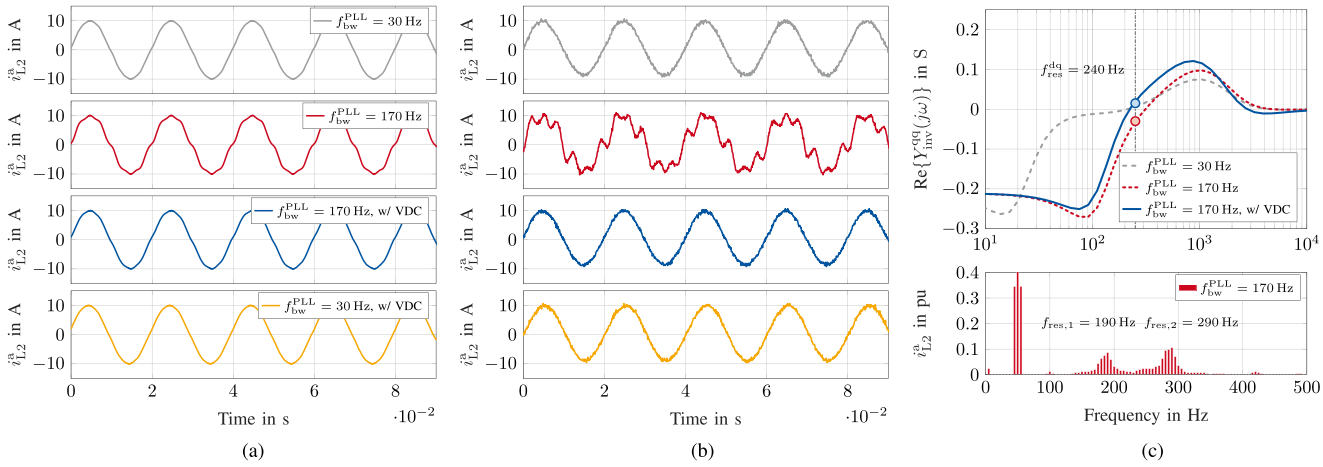

Fig. 22. Validation of case 1. (a) Simulation results. (b) Experiment results. (c) Passivity analysis.

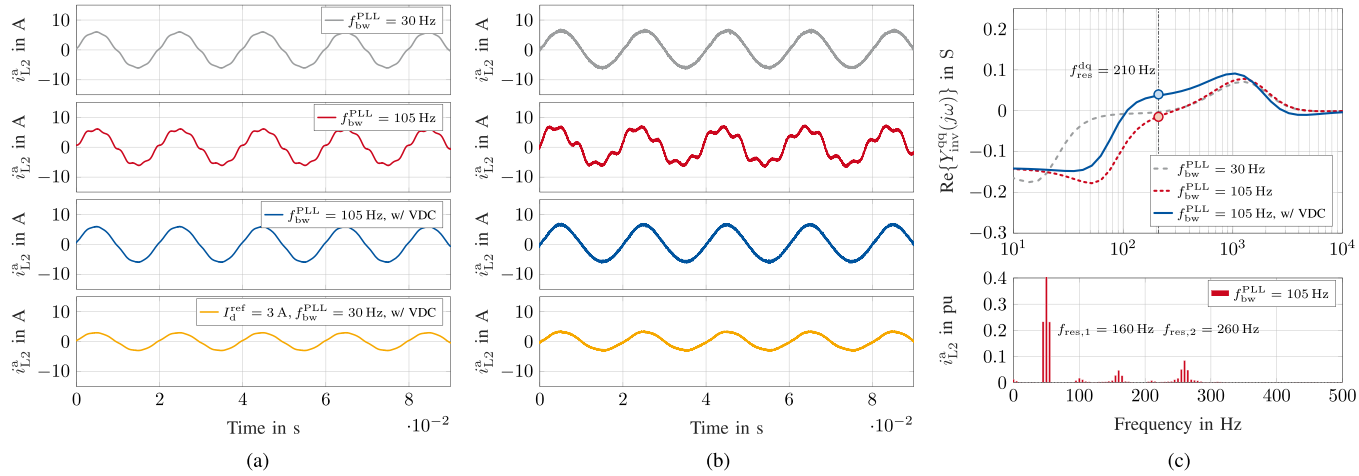

Fig. 23. Validation of case 2. (a) Simulation results. (b) Experiment results. (c) Passivity analysis.

changes toward positive value at the resonant frequency after implementing the VDC, which proves that the resonances can be dissipated through the designed positive damping in the specific frequency range.

B. Case 2

The case 2 validates the effectiveness of the VDC under weak grid operations with SCR $= 4$. Simulation results, experiment results, and passivity analysis are presented in Fig. 23. Unstable resonances measured in experiments occur at 160 and 260 Hz in the abc frame, if the PLL bandwidth increases to 105 Hz, where negative damping is observed in the passivity analysis. After activating the VDC, unstable resonances vanish, since the system behaves passively at the resonant frequency. The VDC applies to the operation with a normal PLL bandwidth and a low current as well.

C. Case 3

The case 3 validates the effectiveness of the VDC with a nonunity power factor, as grid-tied inverters are supposed to operate with a certain amount of reactive current. According to Fig. 10, the injection of reactive currents, either leading or lagging, only slightly affects the passivity of Y_{inv}^{dq}. Both simulations and experiments are conducted considering an operation with PF $= 0.87$ as depicted in Fig. 24, the proposed VDC can reduce the unstable resonances caused by a high PLL bandwidth of 230 Hz in spite of reactive current injections. The frequency-domain analysis of the experiment results matches the passivity analysis. The VDC also works with a normal PLL bandwidth of 30 Hz when injecting reactive currents simultaneously.

D. Case 4

The case 4 validates the necessity to properly design the VDC parameters. The proportional gain K_p^{dd} is preferred to enhance the passivity in the medium-frequency rang. However, an unnecessarily large value should be avoided, which can lead to nonpassive region in the high-frequency range according to Fig. 15. If an unnecessarily high value of K_p^{dd} is implemented, high-frequency resonances are observed in the ac voltage as illustrated in Fig. 25 in both simulations and experiments.

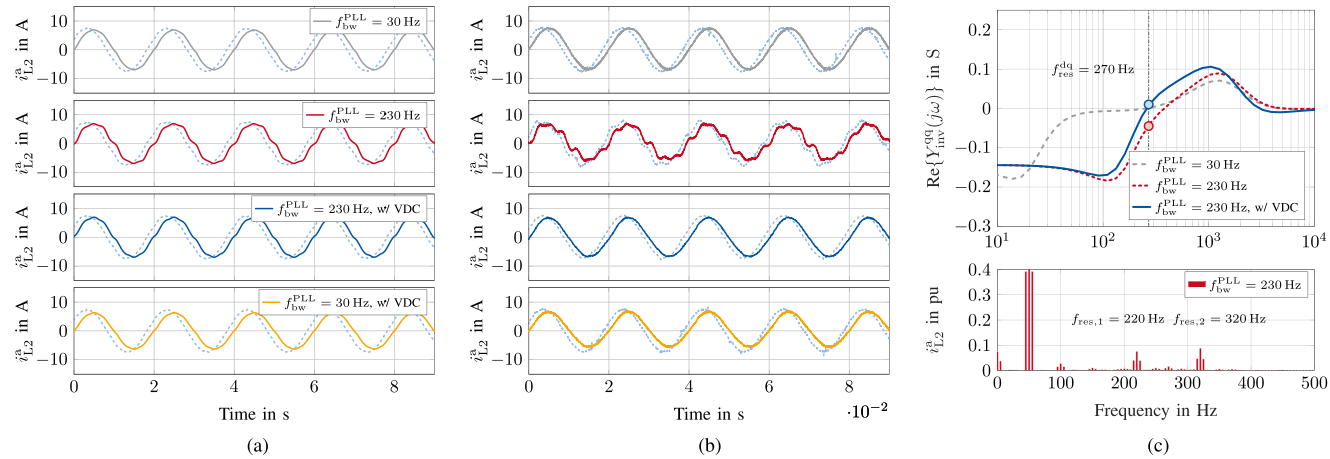

Fig. 24. Validation of case 3 (dotted line: phase voltage of v_C^a). (a) Simulation results. (b) Experiment results. (c) Passivity analysis.

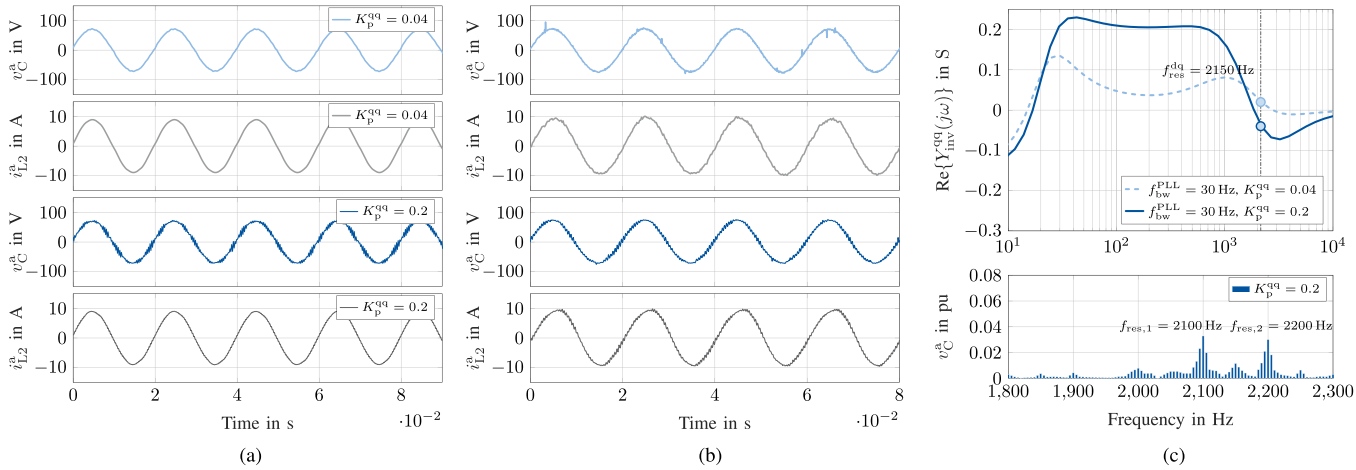

Fig. 25. Validation of case 4. (a) Simulation results. (b) Experiment results. (c) Passivity analysis.

The measured resonances match the nonpassive region estimated by the passivity analysis as well, which indicates that the virtual damping parameters should be carefully designed following the proposed procedure.

VI. Conclusion

This article investigates the stability of a three-phase grid-tied inverter system from the energy dissipation point of view. The damping feature of the system is analyzed intuitively over a wide-frequency range utilizing the two-dimensional passivity properties. The impacts of different control loops and operating conditions are studied, which enables to identify the cause of unstable resonances. To improve the system stability, a VDC is proposed by asymmetrically enhancing the d- and q-axis passivity property. A design approach is provided to determine the virtual damping parameters. The validity of the proposed control method is investigated with both simulations and experiments for different scenarios.

Appendix A
Transfer Function Matrices in IM

Derivations of IM and related transfer function matrices are given as follows. For clarity, real vectors are represented with $x^{dq} = [x^d, x^q]^T$, a small-signal variable is presented with $\hat{x}$, while a steady-state value is described with X.

1) Alternating-Current Control: The dynamic equation in the ACC is given in (11), where m is the modulation index, i_{ref} is the input reference. i_{L1}, i_C, and v_C are measured currents and voltage in the LCL filter. G_{ACC} represents the control matrix of the ACC with a PI controller $F_{\text{ACC}} = K_p^{\text{ACC}} + \frac{K_i^{\text{ACC}}}{s} K_p^{\text{ACC}}$. G_{dec} represents the decoupling transfer matrix, where w_g is the grid frequency. G_{VFF} is the transfer matrix of VFF, where $\omega_{\text{VFF}} = 2\pi f_{\text{bw}}^{\text{VFF}}$ is the bandwidth of VFF. G_{AD} is the transfer matrix of AD, where K_{AD} is the damping factor. G_{del} model the system delay with Páde approximation, where T_{del} includes a computational delay in the digital control (T_{sp}) and a ZOH

effect ($0.5\,T_{\rm sp}$) caused by the PWM

$$\begin{bmatrix} m^{d,c} \\ m^{q,c} \end{bmatrix} \frac{v_{\rm dc}}{2} = G_{\rm del}G_{\rm ACC} \begin{bmatrix} i^{d,c}_{\rm ref} \\ i^{q,c}_{\rm ref} \end{bmatrix} - G_{\rm del}\left(G_{\rm ACC}+G_{\rm dec}\right) \begin{bmatrix} i^{d,c}_{L1} \\ i^{q,c}_{L1} \end{bmatrix} + G_{\rm del}G_{\rm VFF} \begin{bmatrix} v^{d,c}_{C} \\ v^{q,c}_{C} \end{bmatrix} - G_{\rm del}G_{\rm AD} \begin{bmatrix} i^{d,c}_{C} \\ i^{d,c}_{C} \end{bmatrix} \tag{11}$$

$$G_{\rm ACC} = \begin{bmatrix} F_{\rm ACC} & 0 \\ 0 & F_{\rm ACC} \end{bmatrix} \tag{12}$$

$$G_{\rm dec} = \begin{bmatrix} 0 & \omega_g L_1 \\ -\omega_g L_1 & 0 \end{bmatrix} \tag{13}$$

$$G_{\rm VFF} = \begin{bmatrix} \frac{\omega_{\rm VFF}}{s+\omega_{\rm VFF}} & 0 \\ 0 & \frac{\omega_{\rm VFF}}{s+\omega_{\rm VFF}} \end{bmatrix} \tag{14}$$

$$G_{\rm AD} = \begin{bmatrix} K_{\rm AD} & 0 \\ 0 & K_{\rm AD} \end{bmatrix} \tag{15}$$

$$G_{\rm del} = \begin{bmatrix} \frac{2-sT_{\rm del}}{2+sT_{\rm del}} & 0 \\ 0 & \frac{2-sT_{\rm del}}{2+sT_{\rm del}} \end{bmatrix}. \tag{16}$$

2) Phase-Locked Loop: If a PLL is considered, the system will become nonlinear. A linearized small-signal model of the PLL can be derived by considering perturbation quantities. Consider an SRF-based PLL, the transfer function of the PLL small-signal model is given in (17), where $F_{\rm PLL} = K_p^{\rm PLL} + \frac{K_i^{\rm PLL}}{s}$ is the PI controller in the PLL. Influenced by the PLL, variables such as i_{L1}, i_C, v_C are supposed to be converted from the system to control frame when feeding back to control loops, while $v_{\rm ref}$ is required to be converted to the system frame for the PWM modulation. The small-signal relationship between control and system frames are given in (18)–(21)

$$H_{\rm PLL} = \frac{F_{\rm PLL}}{s + V_C^{d,s} F_{\rm PLL}} \tag{17}$$

$$\begin{bmatrix} \hat{i}^{d,c}_{L1} \\ \hat{i}^{q,c}_{L1} \end{bmatrix} = \begin{bmatrix} \hat{i}^{d,s}_{L1} \\ \hat{i}^{q,s}_{L1} \end{bmatrix} + \underbrace{\begin{bmatrix} 0 & I^{q,s}_{L1} H_{\rm PLL} \\ 0 & -I^{d,s}_{L1} H_{\rm PLL} \end{bmatrix}}_{G^{i}_{\rm PLL}} \begin{bmatrix} \hat{v}^{d,s}_{C} \\ \hat{v}^{q,s}_{C} \end{bmatrix} \tag{18}$$

$$\begin{bmatrix} \hat{i}^{d,c}_{C} \\ \hat{i}^{q,c}_{C} \end{bmatrix} = \begin{bmatrix} \hat{i}^{d,s}_{C} \\ \hat{i}^{q,s}_{C} \end{bmatrix} + \underbrace{\begin{bmatrix} 0 & I^{q,s}_{C} H_{\rm PLL} \\ 0 & -I^{d,s}_{C} H_{\rm PLL} \end{bmatrix}}_{G^{\rm ic}_{\rm PLL}} \begin{bmatrix} \hat{v}^{d,s}_{C} \\ \hat{v}^{q,s}_{C} \end{bmatrix} \tag{19}$$

$$\begin{bmatrix} \hat{v}^{d,c}_{C} \\ \hat{v}^{q,c}_{C} \end{bmatrix} = \begin{bmatrix} \hat{v}^{d,s}_{C} \\ \hat{v}^{q,s}_{C} \end{bmatrix} + \underbrace{\begin{bmatrix} 0 & V^{q,s}_{C} H_{\rm PLL} \\ 0 & -V^{d,s}_{C} H_{\rm PLL} \end{bmatrix}}_{G^{v}_{\rm PLL}} \begin{bmatrix} \hat{v}^{d,s}_{C} \\ \hat{v}^{q,s}_{C} \end{bmatrix} \tag{20}$$

$$\begin{bmatrix} \hat{m}^{d,s} \\ \hat{m}^{q,s} \end{bmatrix} = \begin{bmatrix} \hat{m}^{d,c} \\ \hat{m}^{q,c} \end{bmatrix} + \underbrace{\begin{bmatrix} 0 & -M^{q,s} H_{\rm PLL} \\ 0 & M^{d,s} H_{\rm PLL} \end{bmatrix}}_{G^{m}_{\rm PLL}} \begin{bmatrix} \hat{v}^{d,s}_{C} \\ \hat{v}^{q,s}_{C} \end{bmatrix}. \tag{21}$$

3) Direct-Voltage Control: The dynamic equation of the DVC is given in (22), which serves as an input of (11), where $F_{\rm DVC} = K_p^{\rm DVC} + \frac{K_i^{\rm DVC}}{s}$ is the PI controller in the DVC. The small-signal variable $\hat{v}_{\rm dc}$ is influenced by both the modulation index m and ac-side current i_{L1} as given in (24) after linearization, where $Y_{\rm dc} = sC_{\rm dc}$ is the admittance of the dc-link capacitor. Steady-state values of the modulation index are defined in G_M. The steady-state relation of the power balance between the dc and ac sides is given in (25)

$$\begin{bmatrix} i^{d,c}_{\rm ref} \\ i^{q,c}_{\rm ref} \end{bmatrix} = \underbrace{\begin{bmatrix} F_{\rm DVC} \\ 0 \end{bmatrix}}_{G_{\rm DVC}} \left(v_{\rm dc,ref} - v_{\rm dc}\right) \tag{22}$$

$$G_M = \begin{bmatrix} M^d & M^q \end{bmatrix}^T \tag{23}$$

$$\hat{v}_{\rm dc} = \underbrace{\frac{3}{4}\begin{bmatrix} \frac{M^d}{Y_{\rm dc}} & \frac{M^q}{Y_{\rm dc}} \end{bmatrix}}_{G^{i}_{\rm DVC}} \begin{bmatrix} \hat{i}^{d}_{L1} \\ \hat{i}^{q}_{L1} \end{bmatrix} + \underbrace{\frac{3}{4}\begin{bmatrix} \frac{I^d_{L1}}{Y_{\rm dc}} & \frac{I^q_{L1}}{Y_{\rm dc}} \end{bmatrix}}_{G^{m}_{\rm DVC}} \begin{bmatrix} \hat{m}^{d,s} \\ \hat{m}^{q,s} \end{bmatrix} \tag{24}$$

$$V_{\rm dc} I_{\rm pv} = \frac{3}{2} V_C^d I_{L1}^d. \tag{25}$$

4) Filter and Grid: The impedance and admittance of the LCL filter and grid parameters are represented with following matrices

$$Z_{L1} = \begin{bmatrix} sL_1 + R_1 & -\omega_g L_1 \\ \omega_g L_1 & sL_1 + R_1 \end{bmatrix} \tag{26}$$

$$Y_C = \begin{bmatrix} sC & -\omega_g C \\ \omega_g C & sC \end{bmatrix} \tag{27}$$

$$Z_{L2} = \begin{bmatrix} sL_2 + R_2 & -\omega_g L_2 \\ \omega_g L_2 & sL_2 + R_2 \end{bmatrix} \tag{28}$$

$$Z_g = \begin{bmatrix} sL_g + R_g & -\omega_g L_g \\ \omega_g L_g & sL_g + R_g \end{bmatrix}. \tag{29}$$

5) Inverter IM: According to the small-signal relationship, the IM considering the complete system dynamics is given in the following equation

$$Z_{\rm inv} = \frac{\left(\frac{V_{\rm dc} I}{2} - \frac{G_M G^m_{\rm DVC}}{2}\right) G_A^{-1} G_B - \frac{G_M G^i_{\rm DVC}}{2} - Z_{L1}}{\left(\frac{V_{\rm dc} I}{2} - \frac{G_M G^m_{\rm DVC}}{2}\right) G_A^{-1} G_C - I} \tag{30}$$

with

$$G_A = \frac{V_{\rm dc} I}{2} - \frac{G_M G^m_{\rm DVC}}{2} - G_{\rm del} G_{\rm ACC} G_{\rm DVC} G^m_{\rm DVC} \tag{31}$$

$$G_B = G_{\rm del} G_{\rm ACC} G_{\rm DVC} G^i_{\rm DVC} - G_{\rm del}\left(G_{\rm ACC} + G_{\rm dec}\right) + \frac{G_M G^i_{\rm DVC}}{2} \tag{32}$$

$$G_C = \frac{V_{\rm dc} G^m_{\rm PLL}}{2} + G_{\rm del} G_{\rm VFF} G^v_{\rm PLL} - G_{\rm del} G_{\rm AD}\left(G^{\rm ic}_{\rm PLL} + Y_C\right) - G_{\rm del}\left(G_{\rm ACC} + G_{\rm dec}\right) G^i_{\rm PLL}. \tag{33}$$

REFERENCES

[1] C. Li, "Unstable operation of photovoltaic inverter from field experiences," *IEEE Trans. Power Del.*, vol. 33, no. 2, pp. 1013–1015, Apr. 2018.

[2] X. Wang and F. Blaabjerg, "Harmonic stability in power electronic-based power systems: Concept, modeling, and analysis," *IEEE Trans. Smart Grid*, vol. 10, no. 3, pp. 2858–2870, May 2019.

[3] G. Lammert, D. Premm, L. D. P. Ospina, J. C. Boemer, M. Braun, and T. Van Cutsem, "Control of photovoltaic systems for enhanced short-term voltage stability and recovery," *IEEE Trans. Energy Convers.*, vol. 34, no. 1, pp. 243–254, Mar. 2019.

[4] B. Wen, D. Boroyevich, R. Burgos, P. Mattavelli, and Z. Shen, "Analysis of dq small-signal impedance of grid-tied inverters," *IEEE Trans. Power Electron.*, vol. 31, no. 1, pp. 675–687, Jan. 2016.

[5] D. Wang, L. Liang, L. Shi, J. Hu, and Y. Hou, "Analysis of modal resonance between PLL and dc-link voltage control in weak-grid tied VSCs," *IEEE Trans. Power Syst.*, vol. 34, no. 2, pp. 1127–1138, Mar. 2019.

[6] J. Ma, X. Wang, F. Blaabjerg, L. Harnefors, and W. Song, "Accuracy analysis of the zero-order hold model for digital pulse width modulation," *IEEE Trans. Power Electron.*, vol. 33, no. 12, pp. 10826–10834, Dec. 2018.

[7] E. A. A. Coelho, P. C. Cortizo, and P. F. D. Garcia, "Small-signal stability for parallel-connected inverters in stand-alone ac supply systems," *IEEE Trans. Ind. Appl.*, vol. 38, no. 2, pp. 533–542, Mar./Apr. 2002.

[8] N. Pogaku, M. Prodanovic, and T. C. Green, "Modeling, analysis and testing of autonomous operation of an inverter-based microgrid," *IEEE Trans. Power Electron.*, vol. 22, no. 2, pp. 613–625, Mar. 2007.

[9] M. Rasheduzzaman, J. A. Mueller, and J. W. Kimball, "An accurate small-signal model of inverter-dominated islanded microgrids using *dq* reference frame," *IEEE J. Emerg. Sel. Topics Power Electron.*, vol. 2, no. 4, pp. 1070–1080, Dec. 2014.

[10] H. Yuan, X. Yuan, and J. Hu, "Modeling of grid-connected VSCs for power system small-signal stability analysis in dc-link voltage control timescale," *IEEE Trans. Power Syst.*, vol. 32, no. 5, pp. 3981–3991, Sep. 2017.

[11] Z. Yang, Q. Wang, J. Warmuz, and R. W. De Doncker, "Stability assessment of a three-phase grid-tied PV inverter with eigenvalue-based method," in *Proc. IEEE 10th Int. Symp. Power Electron. Distrib. Gener. Syst.*, 2019, pp. 722–727.

[12] J. Sun, "Impedance-based stability criterion for grid-connected inverters," *IEEE Trans. Power Electron.*, vol. 26, no. 11, pp. 3075–3078, Nov. 2011.

[13] X. Wang, L. Harnefors, and F. Blaabjerg, "Unified impedance model of grid-connected voltage-source converters," *IEEE Trans. Power Electron.*, vol. 33, no. 2, pp. 1775–1787, Feb. 2017.

[14] M. Amin and M. Molinas, "Small-signal stability assessment of power electronics based power systems: A discussion of impedance-and eigenvalue-based methods," *IEEE Trans. Ind. Appl.*, vol. 53, no. 5, pp. 5014–5030, Sep./Oct. 2017.

[15] J. Lunze, Regelungstechnik 2: Mehrgrößensysteme, Digitale Regelung. Berlin, Germany: Springer-Verlag, 2010.

[16] J. C. Willems, "Dissipative dynamical systems part i: General theory," *Archive Rational Mech. Anal.*, vol. 45, no. 5, pp. 321–351, 1972.

[17] L. Harnefors, M. Bongiorno, and S. Lundberg, "Input-admittance calculation and shaping for controlled voltage-source converters," *IEEE Trans. Ind. Electron.*, vol. 54, no. 6, pp. 3323–3334, Dec. 2007.

[18] L. Harnefors, L. Zhang, and M. Bongiorno, "Frequency-domain passivity-based current controller design," *IET Power Electron.*, vol. 1, no. 4, pp. 455–465, Dec. 2008.

[19] L. Harnefors, A. G. Yepes, A. Vidal, and J. Doval-Gandoy, "Passivity-based stabilization of voltage-source converters equipped with LCL input filters," in *Proc. 40th Annu. Conf. IEEE Ind. Electron. Soc.*, 2014, pp. 1700–1706.

[20] H.-C. Chen, P.-T. Cheng, and X. Wang, "A passivity-based stability analysis of the active damping technique in the offshore wind farm applications," *IEEE Trans. Ind. Appl.*, vol. 54, no. 5, pp. 5074–5082, Sep./Oct. 2018.

[21] E. Rodriguez-Diaz, F. D. Freijedo, J. M. Guerrero, J.-A. Marrero-Sosa, and D. Dujic, "Input-admittance passivity compliance for grid-connected converters with an LCL filter," *IEEE Trans. Ind. Electron.*, vol. 66, no. 2, pp. 1089–1097, Feb. 2019.

[22] A. Akhavan, H. R. Mohammadi, J. C. Vasquez, and J. M. Guerrero, "Passivity-based design of plug-and-play current-controlled grid-connected inverters," *IEEE Trans. Power Electron.*, vol. 35, no. 2, pp. 2135–2150, Feb. 2020.

[23] L. Harnefors, A. G. Yepes, A. Vidal, and J. Doval-Gandoy, "Passivity-based stabilization of resonant current controllers with consideration of time delay," *IEEE Trans. Power Electron.*, vol. 29, no. 12, pp. 6260–6263, Dec. 2014.

[24] L. Harnefors, R. Finger, X. Wang, H. Bai, and F. Blaabjerg, "VSC input-admittance modeling and analysis above the Nyquist frequency for passivity-based stability assessment," *IEEE Trans. Ind. Electron.*, vol. 64, no. 8, pp. 6362–6370, Aug. 2017.

[25] F. Hans, W. Schumacher, S.-F. Chou, and X. Wang, "Passivation of current-controlled grid-connected VSCs using passivity indices," *IEEE Trans. Ind. Electron.*, vol. 66, no. 11, pp. 8971–8980, Nov. 2019.

[26] H. Zhang, L. Harnefors, X. Wang, H. Gong, and J.-P. Hasler, "Stability analysis of grid-connected voltage-source converters using SISO modeling," *IEEE Trans. Power Electron.*, vol. 34, no. 8, pp. 8104–8117, Aug. 2019.

[27] X. Wang, Y. W. Li, F. Blaabjerg, and P. C. Loh, "Virtual-impedance-based control for voltage-source and current-source converters," *IEEE Trans. Power Electron.*, vol. 30, no. 12, pp. 7019–7037, Dec. 2015.

[28] A. Riccobono and E. Santi, "Positive feedforward control of three-phase voltage source inverter for dc input bus stabilization with experimental validation," *IEEE Trans. Ind. Appl.*, vol. 49, no. 1, pp. 168–177, Jan./Feb. 2013.

[29] J. Fang, X. Li, H. Li, and Y. Tang, "Stability improvement for three-phase grid-connected converters through impedance reshaping in quadrature-axis," *IEEE Trans. Power Electron.*, vol. 33, no. 10, pp. 8365–8375, Oct. 2018.

[30] A. Adib and B. Mirafzal, "Virtual inductance for stable operation of grid-interactive voltage source inverters," *IEEE Trans. Ind. Electron.*, vol. 66, no. 8, pp. 6002–6011, Aug. 2019.

[31] R. Burgos, D. Boroyevich, F. Wang, K. Karimi, and G. Francis, "On the ac stability of high power factor three-phase rectifiers," in *Proc. IEEE Energy Convers. Congr. Expo.*, 2010, pp. 2047–2054.

[32] B. Wen, R. Burgos, D. Boroyevich, P. Mattavelli, and Z. Shen, "Ac stability analysis and dq frame impedance specifications in power-electronics-based distributed power systems," *IEEE J. Emerg. Sel. Topics Power Electron.*, vol. 5, no. 4, pp. 1455–1465, Dec. 2017.

[33] S. Hester, "IEEE 929–2000 Recommended Practice for Utility Interface of Photovoltaic (PV) Systems," *IEEE Std*, 2002.

[34] M. K. Bakhshizadeh *et al.*, "Couplings in phase domain impedance modeling of grid-connected converters," *IEEE Trans. Power Electron.*, vol. 31, no. 10, pp. 6792–6796, Oct. 2016.

Zhiqing Yang (Student Member, IEEE) received the B.S. degree from Southwest Jiaotong University, Chengdu, China, in 2013, and the M.S. degree from RWTH Aachen University, Aachen, Germany, in 2017, both in electrical engineering.

From April to September 2016, he was an Intern with Advanced Technology R&D Center, Mitsubishi Electric, Amagasaki, Japan. In 2017, he joined in the Institute for Power Generation and Storage Systems, E.ON Energy Research Center, RWTH Aachen University, as a Research Associate. His research interests include modeling and control of power electronic system for renewable energy applications.

Chirag Shah (Student Member, IEEE) received the B.Eng. degree in electrical engineering from the Maharaja Sayajirao University of Baroda, Vadodara, India, 2015. He is currently working toward the M.S. degree in electrical engineering with the RWTH Aachen University, Aachen, Germany.

His research interests include modeling and control of renewable energy sources.

Tianxiao Chen (Student Member, IEEE) received the B.S. degree from Zhejiang University, Hangzhou, China, in 2017, and the M.S. degree from RWTH Aachen University, Aachen, Germany, in 2020, both in electrical engineering.

His research interests include stability analysis and improvement, and renewable energy applications.

Jakob Teichrib (Student Member, IEEE) received the M.Sc. degree in electrical engineering from RWTH Aachen University, Aachen, Germany, in 2014.

Since June 2015, he has been a Research Associate with the Institute for Power Generation and Storage Systems (PGS), E.ON Energy Research Center, RWTH Aachen University. His research interests include the field of power semiconductor devices for medium voltage applications.

Rik W. De Doncker (Fellow, IEEE) received the Ph.D. degree in electrical engineering from the Katholieke Universiteit Leuven, Leuven, Belgium, in 1986.

In 1987, he was appointed as a Visiting Associate Professor with the University of Wisconsin, Madison, Madison, WI, USA. After a short stay, as an Adjunct Researcher with Interuniversity Microelectronics Centre, Leuven, Belgium, he joined, in 1989, the Corporate Research and Development Center, General Electric Company, Schenectady, NY, USA. In 1994, he joined Silicon Power Corporation, a former division of General Electric Inc., as the Vice President of technology. In 1996, he became a Professor with RWTH Aachen University, Aachen, Germany, where he currently leads the Institute for Power Electronics and Electrical Drives. Since 2006, he has been the Director of the E.ON Energy Research Center, RWTH Aachen University. In 2009, he led a VDE/ETG Task Force on electric vehicles.

Dr. De Doncker was the President of the IEEE Power Electronics Society (PELS) in 2005 and 2006. He was the Founding Chairman of the German IEEE Industry Applications Society PELS Joint Chapter. In 2002, he was the recipient of the IEEE IAS Outstanding Achievement Award, the IEEE PES Nari Hingorani Custom Power Award, in 2008, the IEEE William E. Newell Power Electronics Award, in 2013, and the IEEE Medal in Power Engineering, in 2020.